# In-situ Quantitative Phase Imaging during Multi-photon Laser Printing

Roman Zvagelsky, Pascal Kiefer, Jannis Weinacker, and Martin Wegener*

ABSTRACT: Shape optimization of microstructures such as microlenses and diffractive optical elements fabricated by multi-photon laser printing is routinely performed by optical characterization after completing printing and development (ex situ). It is, however, highly desirable, instead of or in addition, to optically characterize the samples during the printing process before development (in situ). Here, we successfully demonstrate the integration of in-situ quantitative phase imaging into a commercial multi-photon laser printer. In terms of hardware, this integration merely requires adding illumination by a collimated LED and a small aperture to the existing beam path. In terms of software, we use well-established reconstruction algorithms based on a stack of through-focus, wide-field optical images acquired within a few seconds. We verify this approach by inspecting the topography of various microoptical elements printed with different photoresists and comparing the results with ex-situ measurements obtained by using a spinning-disk confocal optical microscope.
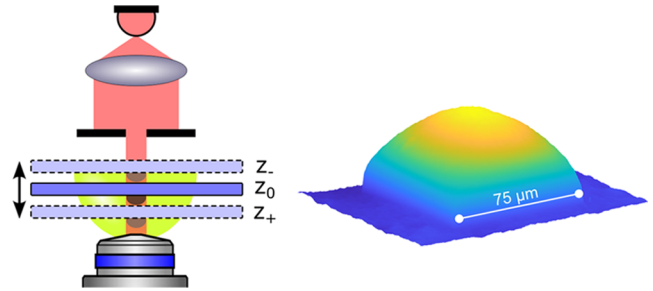
INTRODUCTION

Multi-photon laser printing has become a widely used method for the fabrication of microoptical elements and devices.[1−5] However, measuring the final topography of a printed sample requires removing it from the printing setup, developing it, and analyzing it with a separate imaging tool.[6−8] This process can be time-consuming and challenging, making optimization and quality control of printed microstructures difficult.[9] In-situ measurements, which involve imaging the structure in the same photoresist droplet during printing, offer a potential solution to this problem. In-situ imaging can provide direct access to the sample properties and morphology before the development step, significantly simplifying the optimization procedure. However, a feasible in-situ method for multi-photon laser printing must meet specific requirements: it should be relatively fast, have micrometer resolution, and not cause any undesirable modifications of the printed specimens due to the inspection process.

In recent years, optical coherence tomography (OCT) and optical diffraction tomography (ODT) have been used for in-situ diagnostics during multi-photon laser printing.[10−12] OCT has been demonstrated as a fast in-situ diagnostic tool that can detect specular reflection (or back-scattering) resulting from the refractive index difference between the polymerized material and the monomer.[10] However, this method is effective only for imaging surfaces that are strictly perpendicular to the

optical axis, unless the structure has an additional refractive-index inhomogeneity. ODT is an angle-scanning approach that measures a 2D scattered field and reconstructs it into a 3D refractive index distribution based on certain approximations, typically Born or Rytov.[11,12] Although ODT is a fast 3D reconstruction method, it suffers from the so-called missing cone artifacts and the fact that the inverse problem is mathematically ill-posed.[13,14] These issues significantly deteriorate the quality of the reconstruction, especially for thick samples, and generally do not allow recovery of 3D refractive index distributions for 3D laser-printed specimens.[15] Furthermore, both techniques are interferometric and require highly complex optical setups. Using these setups, which must be perfectly aligned for optimal resolution, can be quite cumbersome.

In this article, we present a non-interferometric approach for in-situ diagnostics during multi-photon laser printing that does not require additional setups and can easily be performed by using the same printing device. Our approach employs
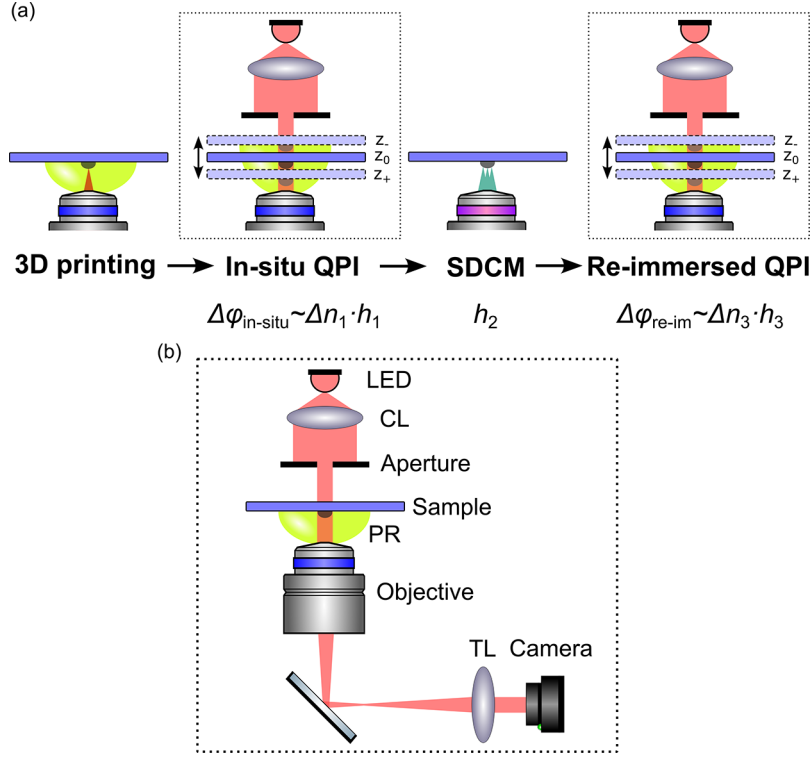
Figure 1. (a) Flowchart illustrating the various steps involved in evaluating the printed structure along with the corresponding measured quantities for each experiment. (b) Scheme of the optical imaging path in Nanoscribe's PPGT and the replaced illumination unit with the collimated LED and aperture. CL = collimating lens, PR = photoresist, TL = tube lens.

quantitative phase imaging (QPI), a wide-field microscopy tool that reconstructs the phase difference between a sample and the medium surrounding it by measuring the phase shift of light after propagation through the specimen along the direction of the optical axis.[16−18] For QPI implementation, we use the so-called transport-of-intensity equation (TIE), which provides access to quantitative phase information with high resolution from intensity measurements.[19,20] This method requires only a through-focus intensity image stack obtained by using spatially coherent illumination.[21] TIE-QPI already has numerous applications in biophotonics and optical metrology, including the measurement of cellular dry mass,[22,23] dynamic cell imaging,[24−26] and the characterization of microlenses and optical fibers.[27,28] To integrate this approach into the laser printing setup, we merely add a collimating lens and a small aperture. We record a set of intensity images taken at different sample positions along the optical axis immediately after laser exposure. Using the TIE numerical solver, we reconstruct the phase difference between the printed structure and the photoresist from the obtained images. To validate the QPI results, we compare them with ex-situ height measurements obtained after sample development using a spinning disk confocal microscope (SDCM). In addition, we apply QPI after sample re-immersion to visualize phase differences that occurred after the development step. Using this three-step approach (in-situ QPI−SDCM−re-immersed QPI), we derive the refractive index of polymer microstructures printed with two different photoresists, relative shrinkage, and measure in-situ topography of printed microoptical elements, such as different diffractive optical elements and microlenses.

EXPERIMENTAL CONFIGURATION AND METHODS

A flowchart depicting the sequence of experiments is presented in Figure 1a. We produce our samples in the dip-in[29] mode of the commercial multi-photon laser printer Photonic Professional GT (PPGT) by Nanoscribe. The setup features a built-in imaging module (Figure 1b) that consists of a tube lens and a camera to capture wide-field images of the printed specimen during the printing process. To incorporate QPI into the printing setup, we substitute the standard transmission illumination unit, which consists of an LED with a diffusor, with a collimated LED (Thorlabs M625L4, central wavelength $\lambda_0 = 630$ nm) and place a small aperture (Thorlabs P900K, diameter $d = 900$ μm) directly onto the sample holder. The aperture provides sufficient spatial coherence of the illuminating light, which is required for the high signal-to-noise ratio of phase reconstruction using TIE. The aperture size does not affect the quality of reconstruction as long as its diameter is smaller than several millimeters.[30] After the laser printing process, we acquire an in-focus image with intensity I_0 (z_0 plane) and 30 out-of-focus images in both directions (z_- and z_+ planes) with a defocus distance of $\Delta z = 2$ μm. The selection of the defocus distance is a trade-off between low-frequency noise (if Δz is too small) and nonlinearity error (if Δz is too big). The chosen value of $\Delta z = 2$ μm lies within the acceptable range.[31] The exposure time of a single frame is 1.4 ms for a 25×/NA0.8 objective and 8 ms for a 63×/NA1.4 objective lens. The acquisition process takes approximately 20 s using the NanoWrite software. Faster data acquisition down to less than 1 s appears possible, provided that direct access to the printer hardware exists.
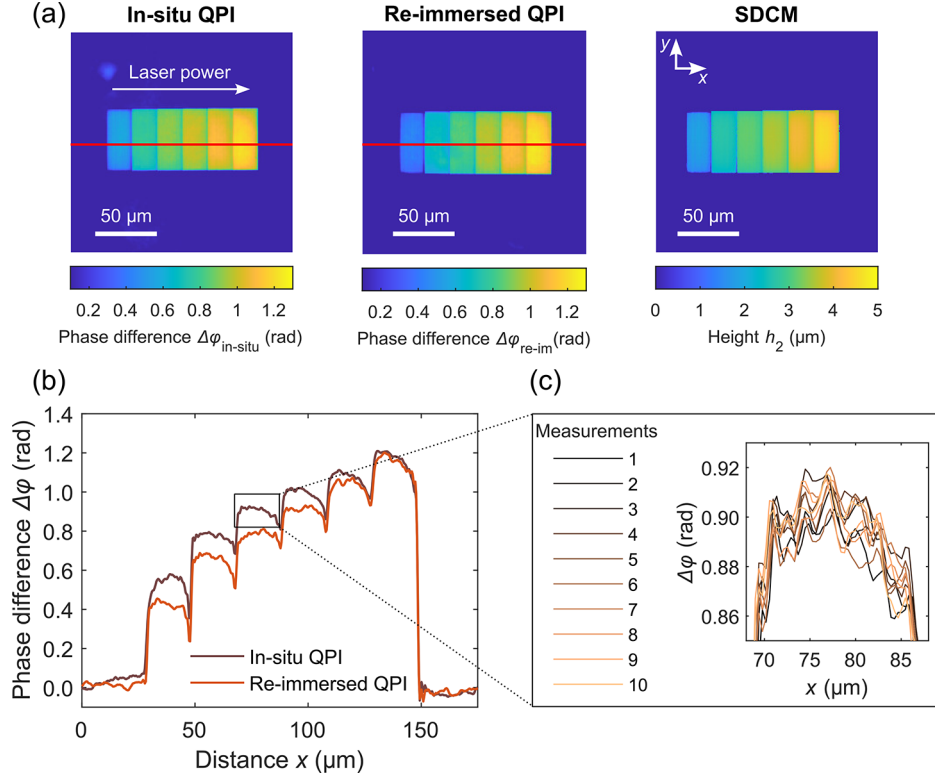
Figure 2. Measurements of IP-S cuboids printed with different laser powers (10−22.5 mW in steps of 2.5 mW). (a) Phase differences measured in situ (left panel) and after development, followed by re-immersion (middle panel) as well as height profiles measured by SDCM after development in the air (right panel). (b) Phase difference profiles obtained by in-situ QPI (brown curve) and by QPI after re-immersion in the same photoresist (orange curve). (c) Ten independent measurements of phase differences of one of the cuboids to test reproducibility.

Thereafter, the image stack containing 61 intensity images is processed using the optimal frequency selection (OFS) algorithm[24,32] to solve the TIE given by

$$-\frac{k}{I_0(\mathbf{r})}\frac{\partial I(\mathbf{r})}{\partial z} = \nabla^2(\Delta\varphi_{\text{in−situ}}(\mathbf{r}))$$

(1)

and obtain the in-situ phase difference between the polymerized material and the unpolymerized photoresist $\Delta\varphi_{\text{in-situ}}$. Here, $k = 2\pi n_{\text{imm}}/\lambda_0$, with refractive index n_{imm} of the immersion liquid used, and $\mathbf{r}$ refers to the lateral 2D spatial coordinate vector. The OFS method consists of three steps. First, we apply a digital Savitzky−Golay differentiation filter with different polynomial degrees for smoothing the data and estimating the intensity derivative $\partial I(\mathbf{r})/\partial z$. Second, we calculate phase distributions by using the fast Fourier transform method[33] to solve eq 1 with the computed intensity derivatives. The final phase difference is then reconstructed from the optimal frequency components of the calculated phase distributions using a filter bank in the spatial frequency domain. It takes 10−40 s to obtain the final 2D phase distribution from the recorded intensity stack depending on the structure size. A more detailed description of the OFS algorithm is available in ref 32.

The phase difference can be expressed in terms of the height of the printed structure $h_1(\mathbf{r})$ and the refractive index difference between the polymer and the monomer Δn_1 as

$$\Delta\varphi_{\text{in−situ}}(\mathbf{r}) = \frac{2\pi\Delta n_1 h_1(\mathbf{r})}{\lambda_0}$$

(2)

After in-situ imaging, we develop structures in propylene glycol methyl ether acetate (PGMEA) for 15 min and in isopropyl alcohol for 5 min and measure their topography $h_2(\mathbf{r})$ in ambient air using SDCM (MarSurf CM expert). To check for changes in the printed object due to the development process, we image the developed sample after re-immersion in the same photoresist. We reconstruct the new phase difference $\Delta\varphi_{\text{re−im}}$ using the same QPI-TIE procedure

$$\Delta\varphi_{\text{re−im}}(\mathbf{r}) = \frac{2\pi\Delta n_3 h_3(\mathbf{r})}{\lambda_0}$$

(3)

RESULTS

Polymer Refractive Index and Shrinkage Evaluation.

We test the proposed in-situ imaging method by investigating different example structures. We start with cuboid blocks printed with different laser powers and hence with different refractive indices. We use the Nanoscribe IP-S photoresist and a 25×/NA0.8 objective lens to print six blocks with a designed volume of $40 \times 10 \times 3$ μm^3. The blocks are printed with a focus scanning speed of 2.5 cm/s. The laser power used for printing is varied from 10 to 22.5 mW in steps of 2.5 mW, covering a laser power range from polymerization to overexposure thresholds. We use a hatching distance of 125 nm and a slicing distance of 300 nm. The reconstructed in situ phase differences $\Delta\varphi_{\text{in-situ}}$, the post-development phase differences after re-immersion $\Delta\varphi_{\text{re−im}}$, and the ex-situ height measurements h_2 are presented in Figure 2a. Line profiles (red lines in Figure 2a) through the reconstructed phases of the printed blocks are depicted in Figure 2b. These profiles show
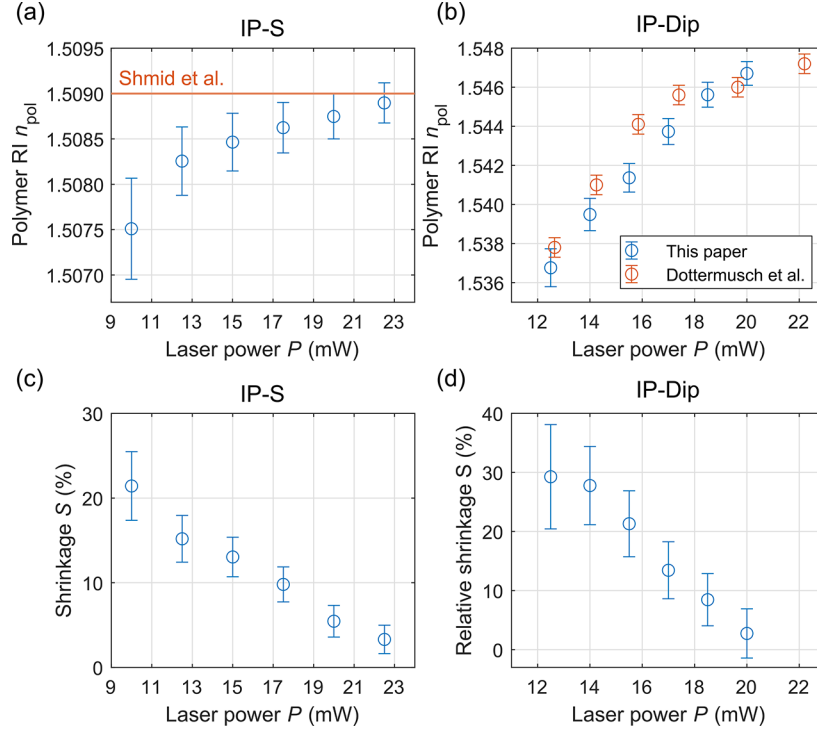
Figure 3. Polymer refractive index and shrinkage as functions of writing laser power under two assumptions: no change in refractive index difference after printing and after re-immersion and no change in height between development and re-immersion. (a) Polymer refractive index versus laser power for Nanoscribe IP-S with the reference value for fully polymerized structures (orange line) from ref 36. (b) Polymer refractive index versus laser power for Nanoscribe IP-Dip with the reference values (orange) from ref 37. (c) Relative shrinkage dependence for IP-S. (d) Relative shrinkage dependence for IP-Dip.

differences in the phase before development (brown curve) and after development, followed by re-immersion (orange curve), which depend on writing laser power and can be interpreted in terms of polymer shrinkage, as will be discussed further below. In addition, we exemplify the stability of the QPI method by measuring the phase profile of one of the blocks 10 times (Figure 2c), leading to a relative standard deviation of less than 1%.

The measured re-immersed phase difference can be recast into the refractive index difference by using eq 3 and two additional assumptions, namely, $\Delta n_1 = \Delta n_3$ and $h_2 = h_3$. These assumptions imply that the refractive index change of the sample after printing and after development followed by re-immersion is the same and that the height of the developed structure remains unchanged after re-immersion. Under these conditions, the refractive index difference can be expressed as

$$\Delta n_1 = \Delta n_3 = \frac{\Delta \varphi_{re-im} \lambda_0}{2\pi h_2} \tag{4}$$

We also print IP-Dip cuboids using a 63×/NA1.4 objective lens and the same writing parameters as for the IP-S structures. The polymer refractive index calculated from eq 4 versus the writing laser power for the photoresists Nanoscribe IP-S and IP-Dip, respectively, is presented in Figure 3a,b. To determine the polymer refractive index, we use the NanoGuide refractive index values of liquid IP-S[34] and IP-Dip,[35] which are equal to $n_{IP-S} = 1.483$ and $n_{IP-Dip} = 1.518$. We compare our obtained refractive index data for the IP-S photoresist with the fully polymerized refractive index value at $\lambda_0 = 630$ nm free-space wavelength from ref 36. For the IP-Dip photoresist, we also

plot polymer refractive index versus laser power from ref 37 obtained for similar structures and wavelengths.

The obtained refractive index dependencies are supported by published data for both photoresists. In the case of IP-S, the observed saturation in the refractive index falls within the range of the reference value for a fully polymerized structure. For IP-Dip, the measured values align with the reference saturation curve within typical variations among different batches of the photoresist.

The phase differences between in-situ QPI and re-immersed QPI in Figure 2b stem from the height change due to polymer shrinkage. Such shrinkage is well known. It occurs when unpolymerized oligomers and unreacted initiators are washed out during the development process. The shrinkage value depends on the degree of polymerization and hence on the writing laser power.[38,39] To estimate the relative shrinkage S, one can use the height ratio after and before development: $S = 1 - h_2/h_1$. Using eqs 3 and 4, this quantity, under the same assumptions, transforms to the phase ratio after re-immersion and after printing: $S = 1 - \Delta \varphi_{re-im}/\Delta \varphi_{in-situ}$. Based on this expression, we calculate the relative shrinkage and plot it versus laser power in Figure 3c,d for both photoresists. The obtained shrinkage values are in the range of 5−30%, which is consistent with the previously reported shrinkage of Nanoscribe photoresists.[40]

Topography Measurements of Printed Microoptical Elements. Next, we apply in-situ QPI for printed microoptical elements. First, we print and evaluate a microlens using a Nanoscribe IP-S photoresist and a 25×/NA0.8 objective lens. For the printing, we use 20 mW laser power, 4 cm/s focus scanning velocity, 50 nm slicing distance, and 100 nm hatching distance. The printed microlens has an aspheric design with a

radius of curvature of 1.03 mm, a conic constant of −2.30, and an overall volume of $75 \times 100 \times 3.9 \ \mu m^3$. To compare QPI and SDCM measurements, we express the phase difference through height using eqs 2 and 3 and the average refractive index difference between the polymer and the photoresist of $\Delta n_{avg} = 0.025$, which is defined in Figure 3a. Microlens topography maps and central profiles for all the three cases (in-situ QPI, ex-situ SDCM, and re-immersed QPI) are presented in Figure 4. For better visibility of measured quantities, we plot
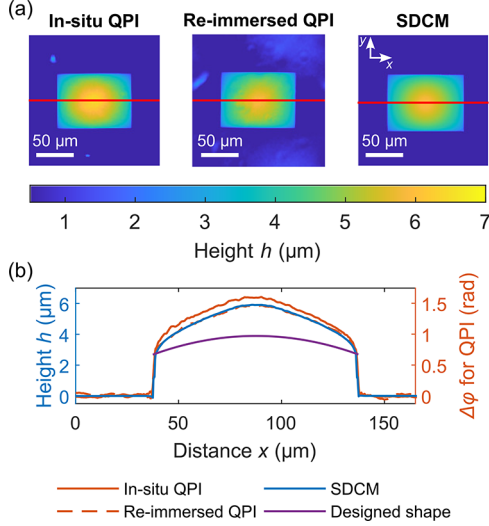

Figure 4. IP-S microlens measurements. (a) Topography maps of a printed microlens. QPI measurements (left and central panels) and the SDCM height profile (right panel) are illustrated using the same false-color scale. Phase differences are expressed through height using the average refractive index difference of $\Delta n_{avg} = 0.025$ (see Figure 3a). (b) Central profiles for in-situ QPI (solid orange curve), re-immersed QPI (dashed orange curve), SDCM height (blue curve), and the designed height (purple curve).

the profiles in Figure 4b using two y-axes. The left axis (blue color) corresponds to the measured height, and the right axis (orange color) corresponds to the measured phase differences. Analyzing the measured data, we observe a slight change in the phase difference of 7% after re-immersion of the sample, caused by shrinkage. The QPI-calculated height profile of the re-immersed sample (dashed orange curve) matches the height measurements obtained by SDCM (blue curve), which additionally confirms the validity of the imaging method. Although the QPI results are in good agreement with the topography measurements, the final height profile differs considerably from the designed value (purple curve). The reason is that the designed height does not take into account the voxel size that can be up to 2.3 μm in the axial direction[10] and that the proximity effect, which refers to the dose accumulation in the vicinity of previously polymerized regions, of the IP-S photoresist is pronounced.[41,42] To solve these issues, the new method of multi-photon grayscale lithography can be applied for printing.[43]

We can also apply the proposed method to printed diffractive optical elements (DOEs). Fabricated by multi-photon laser printing, DOEs are employed for wavefront manipulation in a variety of applications, such as aberration correction for X-ray optics,[44] generating subwavelength focal spot arrays,[45] off-axis holography,[7] etc. In this study, we inspect two DOEs that have been used for multi-focus laser printers.

Using the IP-S resist and the 25×/NA0.8 objective lens, we print and image a single unit cell of the DOE that is designed as a diffractive beam splitter for 7 × 7 foci multi-photon laser printing at high scanning speeds.[46] We use the following parameters for printing: 15 mW laser power, 4 cm/s focus scanning velocity, 85 nm slicing distance, and 100 nm hatching distance. This DOE has a smooth shape, whose measurements are presented in Figure 5a. Phase differences are recalculated to height and are illustrated in the same manner as for the microlens in Figure 4. As shown in Figure 5b, the height profiles of the IP-S DOE for all the three cases (in situ, after development, and after re-immersion) are similar to each other, which means that shrinkage during development is small and less than 5%. Like the microlens, the measured height of the IP-S DOE deviates from the designed value due to the proximity effect and voxel height. Thus, applying in-situ QPI during printing can help to evaluate such deviations from the design and compensate for them on the fly.

Furthermore, we print and evaluate a DOE consisting of several unit cells from ref 47 using the IP-Dip resist and the 63×/NA1.4 objective lens with the following printing parameters: 30 mW laser power, 5 cm/s focus scanning speed, and 145 nm hatching distance. This DOE has only eight different height levels and is used for splitting the beam into 3 × 3 beamlets. Its measured topography is shown in Figure 5c. We use the same refractive index difference of $\Delta n_{avg} = 0.025$, obtained from Figure 3b, as that for IP-S structures to translate phase differences to physical heights. The height profiles of the IP-Dip DOE are depicted in Figure 5d. Herein, the difference between in-situ QPI (solid orange curve) and QPI after re-immersion (dashed orange curve) is also small. The relative shrinkage is less than 5%. We note that, in comparison with the IP-S DOE, the IP-Dip DOE design (purple curve) is originally developed for printing on PPGT and, hence, it already accounts for the finite voxel height. The discrepancy between the designed and measured height values in Figure 5d stems from printing imperfections and is subject of further optimization. Thus, the proposed in-situ QPI method can facilitate and speed up the shape optimization process by partially or completely removing the development step.

DISCUSSION AND CONCLUSIONS

In summary, we have demonstrated that TIE-QPI is a reliable method for examining topography during multi-photon laser printing. The imaging method is inexpensive and can be directly integrated into any laser printing setup by adding a small aperture and a collimated LED. The total time for data acquisition and data evaluation is less than 1 min, making TIE-QPI suitable for routine and fast in-situ monitoring. The obtained phase reconstructions of various designs, such as rectangular blocks, a microlens, and different DOEs, have been validated using ex-situ SDCM height measurements. Performing additional QPI measurements after development and re-immersion in the same photoresist provides valuable information about sample shrinkage, which can then be further used as a feasible method of shrinkage estimation for various photoresists. We believe that QPI can be used regularly for the in-situ inspection of 2.5D structures and on-the-fly optimization of printed microoptics. Moreover, implementing QPI during printing to measure layer-to-layer phase accumulation and use of a priori knowledge of the printed specimen could in the future improve the accuracy of reconstruction and expand possible imaging applications to 3D.
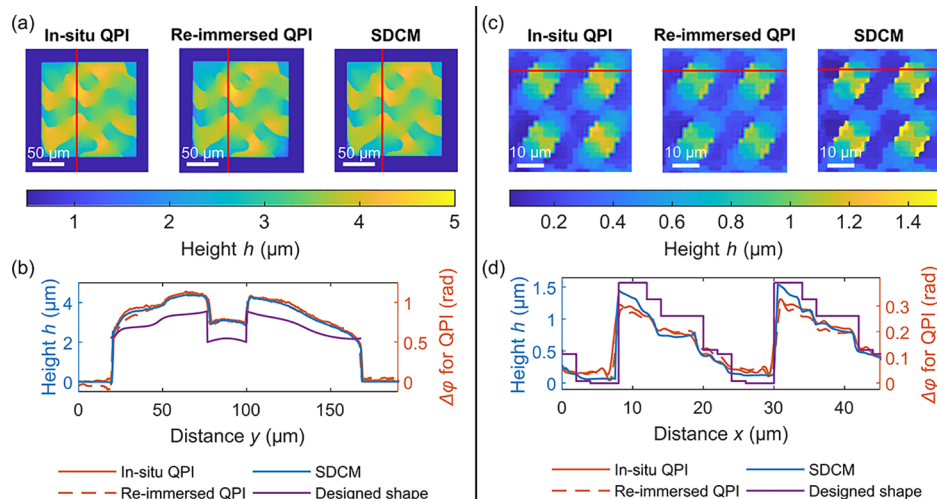
Figure 5. DOE measurements. Phase differences are translated to height using a refractive index difference of $\Delta n_{avg} = 0.025$ (see Figure 3a,b). (a) IP-S DOE[46] topographies for three cases: in-situ QPI, QPI after re-immersion, and SDCM measurements in the air. (b) Height (blue curve) and phase (orange curves) distributions as well as the designed value (purple curve) along the y-cut for IP-S DOE. (c) IP-Dip DOE[47] topographies. (d) Height and phase distributions along the x-cut for IP-Dip DOE. Detailed design of the DOE structures has been presented in refs 46 and 47 and shall not be repeated here.

Although the overall quality of the in-situ phase reconstructions is even comparable to the quality of height measurements obtained by ex-situ SDCM, there are several limitations of the used TIE-QPI method that any user should be aware of:

1. The used OFS algorithm relies on the slowly varying-object approximation, which assumes a small phase change within a small spatial neighborhood.[21,24] Thus, the printed object should not have abrupt phase jumps in the lateral direction. This means one should avoid using this method for imaging structures containing steep slopes or even tall vertical walls.

2. The phase-to-height translation of the printed objects in Figures 4 and 5 assumes that the refractive index difference between the polymer and the monomer is a constant value, which may not be fully true for certain structures. The slight discrepancy between QPI and SDCM height values in Figure 5d might be due to this aspect.

3. During solving the TIE by fast Fourier transform, we imply periodic boundary conditions. This may lead to artifacts at image boundaries if the printed object is larger than the lateral field of view. To address this issue, an additional aperture can be placed in the image plane.[48] However, this solution is not feasible for commercial laser printing setups such as the Nanoscribe PPGT since the manufacturer does not provide free access to the optical beam path behind the objective lens. In contrast, this solution is straightforward to implement in home-built setups.

4. Since TIE-QPI recovers the phase based on the intensity derivative with respect to z, one must be confident that this intensity change arises only from the sample phase. For example, if a printed microlens focuses the incident illumination within the image capture range, the emerging intensity from the focal spot will affect the final phase reconstruction. Another example is oligomer "blobs" in a photoresist that can float in the volume between an objective lens and a substrate.[10] Such

refractive index inhomogeneities are not stable versus time. Therefore, they can produce additional phase noise and artifacts in the phase reconstruction. The background noise in Figure 4a has this origin.

ASSOCIATED CONTENT

Data Availability Statement
The raw intensity data and the QPI-TIE phase reconstruction algorithm will be published in the open-access data repository of Karlsruhe Institute of Technology (10.35097/1004). The used MATLAB code is based on the OFS method published in ref 32.

AUTHOR INFORMATION

Corresponding Author
Martin Wegener − *Institute of Applied Physics (APH), Karlsruhe Institute of Technology (KIT), Karlsruhe, Germany 76131; Institute of Nanotechnology (INT), Karlsruhe Institute of Technology (KIT), Eggenstein-Leopoldshafen, Germany 76344*; Email: martin.wegener@kit.edu

Authors
Roman Zvagelsky − *Institute of Applied Physics (APH), Karlsruhe Institute of Technology (KIT), Karlsruhe, Germany 76131*; orcid.org/0000-0001-9435-2477
Pascal Kiefer − *Institute of Applied Physics (APH), Karlsruhe Institute of Technology (KIT), Karlsruhe, Germany 76131*
Jannis Weinacker − *Institute of Applied Physics (APH), Karlsruhe Institute of Technology (KIT), Karlsruhe, Germany 76131*

REFERENCES

(1) Yang, L.; Mayer, F.; Bunz, U. H. F.; Blasco, E.; Wegener, M. Multi-material multi-photon 3D laser micro- and nanoprinting. *Light: Adv. Manuf.* **2021**, *2*, 296−312.

(2) Toulouse, A.; Drozella, J.; Thiele, S.; Giessen, H.; Herkommer, A. 3D-printed miniature spectrometer for the visible range with a 100 × 100 μm^2 footprint. *Light: Adv. Manuf.* **2021**, *2*, 20−30.

(3) Blaicher, M.; Billah, M. R.; Kemal, J.; Hoose, T.; Marin-Palomo, P.; Hofmann, A.; Kutuvantavida, Y.; Kieninger, C.; Dietrich, P. I.; Lauermann, M.; et al. Hybrid multi-chip assembly of optical communication engines by in situ 3D nano-lithography. *Light: Sci. Appl.* **2020**, *9*, 71.

(4) Wang, H.; Wang, H.; Zhang, W.; Yang, J. K. W. Toward Near-Perfect Diffractive Optical Elements via Nanoscale 3D Printing. *ACS Nano* **2020**, *14*, 10452−10461.

(5) Gonzalez-Hernandez, D.; Varapnickas, S.; Bertoncini, A.; Liberale, C.; Malinauskas, M. Micro-Optics 3D Printed via Multi-Photon Laser Lithography. *Adv. Opt. Mater.* **2023**, *11*, 2201701.

(6) Weber, K.; Hütt, F.; Thiele, S.; Gissibl, T.; Herkommer, A.; Giessen, H. Single mode fiber based delivery of OAM light by 3D direct laser writing. *Opt. Express* **2017**, *25*, 19672−19679.

(7) Wang, H.; Liu, Y.; Ruan, Q.; Liu, H.; Ng, R. J. H.; Tan, Y. S.; Wang, H.; Li, Y.; Qiu, C.; Yang, J. K. W. Off-Axis Holography with Uniform Illumination via 3D Printed Diffractive Optical Elements. *Adv. Opt. Mater.* **2019**, *7*, 1900068.

(8) Hahn, V.; Messer, T.; Bojanowski, N. M.; Curticean, E. R.; Wacker, I.; Schröder, R. R.; Blasco, E.; Wegener, M. Two-step absorption instead of two-photon absorption in 3D nanoprinting. *Nat. Photonics* **2021**, *15*, 932−938.

(9) Siegle, L.; Ristok, S.; Giessen, H. Complex aspherical singlet and doublet microoptics by grayscale 3D printing. *Opt. Express* **2023**, *31*, 4179−4189.

(10) Zvagelsky, R.; et al. Towards *in-situ* diagnostics of multi-photon 3D laser printing using optical coherence tomography. *Light: Adv. Manuf.* **2022**, *3*, 466−480.

(11) He, Y.; Shao, Q.; Chen, S.-C.; Zhou, R. Characterization of two-photon photopolymerization fabrication using high-speed optical diffraction tomography. *Addit. Manuf.* **2022**, *60*, 103293.

(12) Bianchi, S.; Brasili, F.; Saglimbeni, F.; Cortese, B.; Di Leonardo, R. Optical diffraction tomography of 3D microstructures using a low coherence source. *Opt. Express* **2022**, *30*, 22321−22332.

(13) Lim, J.; Lee, K.; Jin, K. H.; Shin, S.; Lee, S.; Park, Y.; Ye, J. C. Comparative study of iterative reconstruction algorithms for missing cone problems in optical diffraction tomography. *Opt. Express* **2015**, *23*, 16933.

(14) Lee, M.; Hugonnet, H.; Park, Y. Inverse problem solver for multiple light scattering using modified Born series. *Optica* **2022**, *9*, 177−182.

(15) Ziemczonok, M.; Kuś, A.; Kujawińska, M. Optical diffraction tomography meets metrology — Measurement accuracy on cellular and subcellular level. *Measurement* **2022**, *195*, 111106.

(16) Park, Y.; Depeursinge, C.; Popescu, G. Quantitative phase imaging in biomedicine. *Nat. Photonics* **2018**, *12*, 578−589.

(17) Nguyen, T. L.; Pradeep, S.; Judson-Torres, R. L.; Reed, J.; Teitell, M. A.; Zangle, T. A. Quantitative Phase Imaging: Recent Advances and Expanding Potential in Biomedicine. *ACS Nano* **2022**, *16*, 11516−11544.

(18) Popescu, G. *Quantitative Phase Imaging of Cells and Tissues*; McGraw-Hill Education, 2011.

(19) Teague, M. R. Deterministic phase retrieval: a Green's function solution. *J. Opt. Soc. Am.* **1983**, *73*, 1434−1441.

(20) Streibl, N. Phase imaging by the transport equation of intensity. *Opt. Commun.* **1984**, *49*, 6−10.

(21) Zuo, C.; Li, J.; Sun, J.; Fan, Y.; Zhang, J.; Lu, L.; Zhang, R.; Wang, B.; Huang, L.; Chen, Q. Transport of intensity equation: a tutorial. *Opt Laser. Eng.* **2020**, *135*, 106187.

(22) Phillips, K.; Velasco, C. R.; Li, J.; Kolatkar, A.; Luttgen, M.; Bethel, K.; Duggan, B.; Kuhn, P.; McCarty, O. J. T. Optical Quantification of Cellular Mass, Volume, and Density of Circulating Tumor Cells Identified in an Ovarian Cancer Patient. *Front. Oncol.* **2012**, *2*, 72.

(23) Phillips, K. G.; Jacques, S. L.; McCarty, O. J. T. Measurement of Single Cell Refractive Index, Dry Mass, Volume, and Density Using a Transillumination Microscope. *Phys. Rev. Lett.* **2012**, *109*, 118105.

(24) Zuo, C.; Chen, Q.; Qu, W.; Asundi, A. High-speed transport-of-intensity phase microscopy with an electrically tunable lens. *Opt. Express* **2013**, *21*, 24060−24075.

(25) Li, Y.; Di, J.; Wu, W.; Shang, P.; Zhao, J. Quantitative investigation on morphology and intracellular transport dynamics of migrating cells. *Appl. Opt.* **2019**, *58*, G162−G168.

(26) Zuo, C.; Chen, Q.; Qu, W.; Asundi, A. Noninterferometric single-shot quantitative phase microscopy. *Opt. Lett.* **2013**, *38*, 3538−3541.

(27) Zuo, C.; Chen, Q.; Li, H.; Qu, W.; Asundi, A. Boundary-artifact-free phase retrieval with the transport of intensity equation II: applications to microlens characterization. *Opt. Express* **2014**, *22*, 18310−18324.

(28) Jenkins, M. H.; Long, J. M.; Gaylord, T. K. Multifilter phase imaging with partially coherent light. *Appl. Opt.* **2014**, *53*, D29−D39.

(29) Bückmann, T.; Stenger, N.; Kadic, M.; Kaschke, J.; Frölich, A.; Kennerknecht, T.; Eberl, C.; Thiel, M.; Wegener, M. Tailored 3D Mechanical Metamaterials Made by Dip-in Direct-Laser-Writing Optical Lithography. *Adv. Mater.* **2012**, *24*, 2710−2714.

(30) Bellair, C. J.; Curl, C. L.; Allman, B. E.; Harris, P. J.; Roberts, A.; Delbridge, L. M. D.; Nugent, K. A. Quantitative phase amplitude microscopy IV: imaging thick specimens. *J. Microsc.* **2004**, *214*, 62−69.

(31) Martinez-Carranza, J.; Falaggis, K.; Kozacki, T. Optimum measurement criteria for the axial derivative intensity used in transport of intensity-equation-based solvers. *Opt Lett.* **2014**, *39*, 182−185.

(32) Zuo, C.; Chen, Q.; Yu, Y.; Asundi, A. Transport-of-intensity phase imaging using Savitzky-Golay differentiation filter - theory and applications. *Opt. Express* **2013**, *21*, 5346−5362.

(33) Gureyev, T. E.; Nugent, K. A. Rapid quantitative phase imaging using the transport of intensity equation. *Opt. Commun.* **1997**, *133*, 339−346.

(34) IP-S Tables. NanoGuide https://support.nanoscribe.com/hc/en-gb/articles/360009156133-IP-S-Tables (accessed June 13, 2023).

(35) IP-Dip Tables. NanoGuide https://support.nanoscribe.com/hc/en-gb/articles/360009156293-IP-Dip-Tables (accessed June 13, 2023).

(36) Schmid, M.; Ludescher, D.; Giessen, H. Optical properties of photoresists for femtosecond 3D printing: refractive index, extinction, luminescence-dose dependence, aging, heat treatment and comparison between 1-photon and 2-photon exposure. *Opt. Mater. Express* **2019**, *9*, 4564−4577.

(37) Dottermusch, S.; Busko, D.; Langenhorst, M.; Paetzold, U. W.; Richards, B. S. Exposure-dependent refractive index of Nanoscribe IP-Dip photoresist layers. *Opt. Lett.* **2019**, *44*, 29−32.

(38) Denning, R. G.; Blanford, C. F.; Urban, H.; Bharaj, H.; Sharp, D. N.; Turberfield, A. J. The Control of Shrinkage and Thermal Instability in SU-8 Photoresists for Holographic Lithography. *Adv. Funct. Mater.* **2011**, *21*, 1593−1601.

(39) Bauer, J.; Guell Izard, A.; Zhang, Y.; Baldacchini, T.; Valdevit, L. Programmable Mechanical Properties of Two-Photon Polymerized Materials: From Nanowires to Bulk. *Adv. Mater. Technol.* **2019**, *4*, 1900146.

(40) Bauer, J.; Izard, A. G.; Zhang, Y.; Baldacchini, T.; Valdevit, L. Thermal post-curing as an efficient strategy to eliminate process parameter sensitivity in the mechanical properties of two-photon polymerized materials. *Opt. Express* **2020**, *28*, 20362−20371.

(41) Glöckler, F.; Hausladen, F.; Alekseenko, I.; Gröger, A.; Pedrini, G.; Claus, D. Two-photon-polymerization enabled and enhanced multi-channel fibre switch. *Eng. Res. Express* **2021**, *3*, 045016.

(42) Kiefer, P.; Hahn, V.; Nardi, M.; Yang, L.; Blasco, E.; Barner-Kowollik, C.; Wegener, M. Sensitive Photoresists for Rapid Multi-photon 3D Laser Micro- and Nanoprinting. *Adv. Opt. Mater.* **2020**, *8*, 2000895.

(43) Rodríguez, S. Redefining Microfabrication of High-Precision Optics. *PhotonicsViews* **2020**, *17*, 36−39.

(44) Seiboth, F.; Kubec, A.; Schropp, A.; Niese, S.; Gawlitza, P.; Garrevoet, J.; Galbierz, V.; Achilles, S.; Patjens, S.; Stuckelberger, M. E.; et al. Rapid aberration correction for diffractive X-ray optics by additive manufacturing. *Opt. Express* **2022**, *30*, 31519−31529.

(45) Jiang, M.; Song, S.; Li, Y.; Zeng, X.; Zhu, L.; Zhang, M.; Wang, S.; Li, X.; Cao, Y. 3D high precision laser printing of a flat nanofocalizer for subwavelength light spot array. *Opt. Lett.* **2021**, *46*, 356−359.

(46) Kiefer, P.; Hahn, V.; Wegener, M. A 7 × 7-foci 3D laser nanoprinter using a diffractive optical element and an aspheric-lens array made by 3D laser nanoprinting. *Proceedings of SPIE PC12412*, 2023.

(47) Hahn, V.; Kiefer, P.; Frenzel, T.; Qu, J.; Blasco, E.; Barner-Kowollik, C.; Wegener, M. Rapid Assembly of Small Materials Building Blocks (Voxels) into Large Functional 3D Metamaterials. *Adv. Funct. Mater.* **2020**, *30*, 1907795.

(48) Zhang, J.; Chen, Q.; Sun, J.; Tian, L.; Zuo, C. On a universal solution to the transport-of-intensity equation. *Opt. Lett.* **2020**, *45*, 3649−3652.